Materials Research. 2020; 23(3): e20200061
DOI: https://doi.org/10.1590/1980-5373-MR-2020-0061

Photoluminescence, Photoacoustic and Structural Characteristics of Polycrystalline Zn_2TiO_4: Ni^{2+} Semiconductor

*L. P. V. Gomes[a,b], S. S. Pedro[a], A. López[a], A. R. Camara[a], N. Cella[c], L. P. Sosman[a]**

[a]*Universidade do Estado do Rio de Janeiro, Instituto de Física, Rua São Francisco Xavier, 524, 20550-900, Rio de Janeiro, RJ, Brasil*
[b]*Universidade Estadual de Montes Claros, Centro de Ciência Exatas e Tecnológicas, Av. Prof. Rui Braga, 46, 39401-089, Montes Claros, MG, Brasil*
[c]*Universidade do Estado do Rio de Janeiro, Instituto Politécnico, 28601-970, Nova Friburgo, RJ, Brasil*

Received: February 12, 2020; Revised: May 26, 2020; Accepted: May 27, 2020

This work presents the investigation, at room temperature, of Zn_2TiO_4 samples containing Ni^{2+} ions as substitutional impurities. Samples with molecular formula $Zn_{2(1-x)}Ni_{2x}TiO_4$, where x = 0.00, 0.0007, 0.001, 0.0013, 0.002 and 0.003, in which Zn^{2+} ions were replaced by Ni^{2+} ions, were prepared through solid-state method, crystalline data were obtained by X-ray diffraction, the elemental composition was determined by X-ray fluorescence and the optical properties were investigated through photoluminescence and photoacoustic techniques. The photoluminescence spectra showed broadbands from 640 nm to 800 nm. The emission of the $Zn_{2(1-x)}Ni_{2x}TiO_4$ samples was assigned to the overlapping of the Ni^{2+} and the Zn_2TiO_4 emission. The most intense photoluminescence signal was obtained with excitation radiation at a wavelength of 360 nm for the sample with x = 0.001. The photoacoustic spectra showed absorption bands characteristic of semiconductor materials due to the host Zn_2TiO_4. The energy bandgap of the $Zn_{2(1-x)}Ni_{2x}TiO_4$ was obtained from photoacoustic absorption spectra.

Keywords: Photoluminescence, photoacoustic; Ni^{2+}; semiconductor material.

1. Introduction

Zn_2TiO_4 is a spinel-type compound, in which the Zn^{2+} ions are randomly distributed in tetrahedral and octahedral sites, while the Ti^{4+} ions are in octahedral sites[1]. This compound presents interesting characteristics for different applications, such as photocatalytic material, used for degradation of organic pollutants, (for example, pesticides) in water[2]. The basic photocatalytic process consists of the irradiation of Zn_2TiO_4 particles with energy higher than the bandgap, generating electron-hole pairs. This system starts chemical reactions capable of mineralizing the organic pollutants, in a similar way to photocatalytic degradation produced by TiO_2 of the Microcystin-LR (MC-LR), which is a toxin produced by cyanobacteria[3]. Other examples of Zn_2TiO_4 applications are dielectric resonators in microwave devices[4,5] used in ultra-high-frequency range for wireless communications, since the compound presents a low dielectric constant and high-quality factor[6]. Microwave dielectric properties of Zn_2TiO_4 and Zn_2TiO_4+TiO_2 were discussed in reference[7], where the dependence of dielectric constant with a quantity of TiO_2 in the sample can be seen. Some works also report the system in use as white color pigment[8].

Another important characteristic is the photoluminescence observed from $Zn_{2(1-x)}Ni_{2x}TiO_4$. When the host cations are substituted by transition metal ions, the Zn_2TiO_4 can present broadbands in the visible and near-infrared region at room temperature. For example, the photoluminescence at room temperature of the Zn_2TiO_4 obtained through solid-state method presents a broad and intense band from 680 nm to 800 nm[8,9]. Zn_2TiO_4:Co^{2+} shows a broadband in the red-infrared region characteristic of Co^{2+} ions in tetrahedral sites[10], and when the host contains substitutional Mn^{2+} ions the system presents two bands in the green and red regions due to electronic transitions of the Mn^{2+} ions in tetrahedral and octahedral sites, respectively[9]. Zn_2TiO_4 also presents a reddish-orange luminescence when lanthanides like Sm^{3+} ions are inserted in the host[11]. Apart from the several interesting properties, Zn_2TiO_4 can be easily obtained through the conventional solid-state reaction of 2ZnO-TiO_2 without any additional sintering processes[8-10].

The optical properties of Ni^{2+} have been investigated for many years. For example, the MgO: Ni^{2+} was identified as an excellent tunable solid-state laser system[12], systems MgF_2:Ni^{2+} (emitting from 1610 nm to 1740 nm at 80 K) and $Gd_3Ga_5O_{12}$:Ni^{2+} (emitting from 1434 nm to 1520 nm at 100 K)[13] were classified as laser materials, but the lasing action in these materials occur at low temperature. Nowadays Ni^{2+}-doped transparent nanoglass ceramics (nano-GC) containing Ga_2O_3 nanocrystals have been investigated by ultra-broadband emission at the near-infrared region due to the addition of Nd^{3+} and Yb^{3+}, because energy-transfer processes result in an enhancement of Ni^{2+} emission[14]. The $ZnGa_2O_4$:Ni^{2+} inserted in glass-ceramics showed a strong near-infrared emission, pointing to a promising use as broadband fiber amplifiers[15]. Beyond near-infrared emission, materials containing Ni^{2+} impurities also present emission in the visible region. For example, photoluminescence spectra in blue, green and red regions were observed in $Y(OH)_3$:Ni^{2+} and cubic Y_2O_3:Ni^{2+} phosphors[16], violet and blue emissions were observed in polyvinyl alcohol cadmium telluride nanoparticles containing Ni^{2+} [17], and an

*e-mail: sosman@uerj.br

emission in the red region was observed in $MgGa_2O_4:Ni^{2+}$ [18]. In addition to the near-infrared emission, the Ni^{2+} ion is very stable, therefore, valence changes during thermal processes are not expected. As a consequence, valence control is not necessary during materials synthesis, which means atmosphere control is expendable during the thermal processes[19].

Besides the achievement of the emission and excitation bands, the determinations of the valence state and of the type of substitutional element are also necessary to understand quantum processes in an emitting sample. Photoluminescence is a very appropriate technique for these, because it is 10^4 times more sensitive than others techniques that are also capable of revealing this information, as the X-ray photoelectron spectroscopy (XPS), for example[20,21]. Therefore, in this paper the photoluminescence was the technique used to confirm both, the type and the valence of the emitting substitutional ion, besides the symmetry of the occupation site.

By the facile production of the semiconductor Zn_2TiO_4, together with photoluminescence possibilities from Ni^{2+} substitution, this work reports on the $Zn_2TiO_4:Ni^{2+}$ produced by the solid-state method and its investigation through X-ray diffraction, photoluminescence, excitation, and photoacoustic spectroscopies at room temperature. This investigation was motivated by the application possibility of the broadband observed in a potential lasing system at room temperature.

2. Materials and Methods

Samples with molecular formula $Zn_{2(1-x)}Ni_{2x}TiO_4$, where x = 0.00, 0.0007, 0.001, 0.0013, 0.002, and 0.003, respectively, were prepared through solid-state method using raw compounds ZnO (Carlo Erba), TiO_2 (B. Herzog), and $Ni(OH)_2$ (Sigma Aldrich). The components of each sample were weighted in accordance with the desired stoichiometric reaction and mixed into an agate mortar to produce a homogeneous powder. During the next step, each admixture powder was pressed under 4 t into three pellets, with 13 mm diameter and 2 mm thickness, with a mass of about 0.7 g. The pellets were put into alumina crucibles and heated in an atmospheric pressure oven at 1200 °C for 6 hours. The oven was turned off and the samples were cooled to room temperature by furnace inertia. The $Zn_{2(1-x)}Ni_{2x}TiO_4$, where x = 0.00, presented a slight yellow color while the $Zn_{2(1-x)}Ni_{2x}TiO_4$, where x = 0.0007, 0.001, 0.0013, 0.002 and 0.003 presented a green color. The concentration of Ni^{2+} in the samples is the fraction of zinc (Zn^{2+}) ions which have been replaced with nickel (Ni^{2+}) ions.

The sample coloration is formed by the components of visible light, which are not absorbed in the sample surface. The observed color is the "complementary color" of the absorbed radiation. The yellow color of Zn_2TiO_4 pure sample (without Ni^{2+}) is due to the absorption at the sample surface, of the wavelengths in the blue region of the spectrum. Since blue and yellow are complementary colors, the yellow color is reflected in sample surface, reaching the detector (eyes)[22]. The color of Ni^{2+}-samples will be explained in more details in the Results section.

The X-ray diffraction was acquired at room temperature by a Bruker D2-PHASER powder-diffractometer (40kV, 40mA) using Cu-Kα_1 radiation with a wavelength of 1.5406 Å. The obtained data were refined by the Rietveld method using the FullProf package[23] and a pseudo-Voigt (pV) profile function to fit the diffracted peaks. The data were compared with the ICSD (Inorganic Crystal Structure Database)[24]. Lattice parameters and atomic positions were determined from the refinement.

The X-ray fluorescence measurements were obtained by an Artax 200 X-Ray Fluorescence Spectrometer (30 kV, 200 μA, and a molybdenum anode) and used to identify the atomic elements present in the samples.

The measurements of time-resolved photoluminescence and excitation were performed with a spectrofluorometer PTI QuantaMaster 300-Plus equipped with a 75 W pulsed Xenon lamp with a spectral resolution of 2 nm in the visible region. For phase-resolved photoluminescence measurements, an Acton AM 510 spectrometer with a spectral resolution of 1 nm was used. The excitation source was a 532 nm, 50 mW Coherent Compass 215M laser, modulated by a Newport 75160 variable speed chopper. The signal was detected by a Newport Oriel 77348 photomultiplier, amplified and analyzed with a Princeton 5209 lock-in. The scattered excitation light was blocked with Newport optical filters.

The photoacoustic spectra were obtained using a Newport 300 W Xe lamp as the radiation source and an Oriel 77200 monochromator with a spectral resolution of 10 nm to select the excitation wavelength. An Oriel Model 75095 chopper was used for the lamp light chopping at 10 Hz. The signal was detected with a B&K model 4943 microphone in a homemade photoacoustic cell with a quartz window. The signal analysis was done with a Stanford Research Systems Model SR830 lock-in amplifier. All spectra were corrected by the response of the detection system.

3. Results

Figure 1 shows the X-ray diffraction and the Rietveld refinements results for the $Zn_{2(1-x)}Ni_{2x}TiO_4$, where x = 0.00, 0.0007, 0.001, 0.0013, 0.002 and 0.003. The circles represent

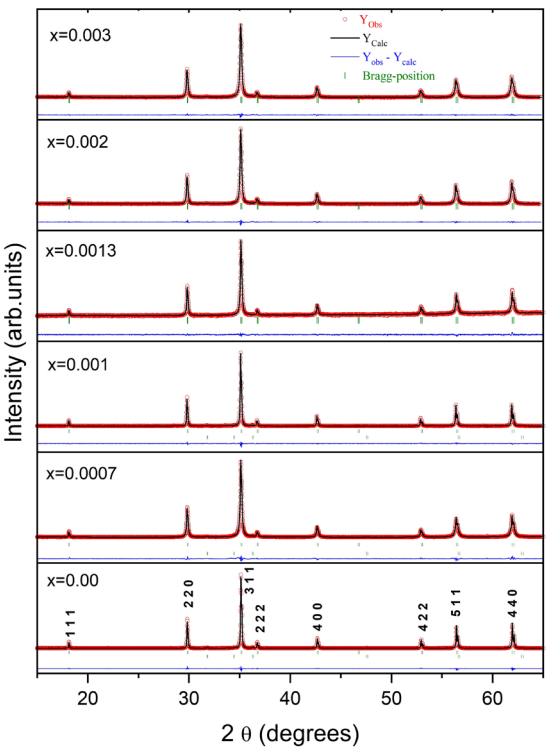

Figure 1. Room temperature X-ray diffraction and Rietveld refinement results of $Zn_{2(1-x)}Ni_{2x}TiO_4$, where x = 0.00, 0.0007, 0.001, 0.0013, 0.002 and 0.003. Bragg positions are related to the Zn_2TiO_4 (top) and ZnO (bottom) phases.

the measured data and the solid line represents the adjustment obtained from a pseudo-Voight function of Rietveld refinements. The first set of sticks (at the top) indicates the Bragg diffraction positions of Zn_2TiO_4, and the second set of sticks (at the bottom) is related to the Bragg diffraction positions of the ZnO phase. The bottom horizontal solid line is the difference between the measured diffraction and the calculated data obtained from Zn_2TiO_4 PDF 860156 (ICSD 080851)[25] and ZnO PDF 800075 (ICSD 067849)[26]. Results from X-ray data refinements are exhibited in Tables 1 and 2.

The GOF-index (Goodness-of-Fit) indicates the discrepancy between the observed and expected values of X-ray diffraction data. The desired value of the GOF-index is 1.0[23]. The values for the $Zn_{2(1-x)}Ni_{2x}TiO_4$, where x =0.00, 0.0007, 0.001, 0.0013, 0.002 and 0.003, obtained from the Rietveld refinement indicate the correct identification of the sample phase(s) and of the crystallographic structure (space group). Table 1 shows that for the investigated Ni^{2+} concentration interval, the space group, the cell parameter and the cell volume are not significantly affected when the Ni^{2+} ion is introduced in the host. This fact can be explained by the low Ni^{2+} concentration of the sample. The lattice parameters obtained from Rietveld refinements (Table 1) indicate samples with a cubic (face-centered) space group. Due to the small difference between the values shown in Table 1 (< 0.3%), the cell volume of Zn_2TiO_4 and $Zn_{2(1-x)}Ni_{2x}TiO_4$ samples can be considered unchanged when Ni^{2+} ion is inserted in the host[27].

Table 1 also shows the values of crystallite size (D), micro-strain (ε) and dislocation density (δ) parameters for all samples, obtained from X-ray diffraction measurements[28,29]. It can be seen that the crystallite size decreases when the Ni^{2+} concentration increases while micro-strain and dislocation density increase with the increasing of Ni^{2+} concentration, except for the 0.07% sample. The decrease of the average crystallite size with the increasing of the impurity ion concentration is related with a worsens of the crystallinity of samples[28]. Besides this, the micro-strain and dislocation density parameters reflect in the same way the crystalline quality of samples[30]. Table 1 shows that the dislocation density increases with Ni^{2+} concentration, which reflects an increasing of lattice imperfections due to the increase of micro-strains in the samples[31]. Therefore, the increasing of the dislocation density and of the micro-strain in the samples is in accordance with the decreasing of crystallite size, indicating a lower crystalline quality of the Zn_2TiO_4:Ni^{2+}samples when compared to the Zn_2TiO_4 sample. The changes in these specific crystal parameters are associated with the ionic radii differences between host ion Zn^{2+} and the substitutional impurity Ni^{2+}, which inserts small defects in the host, however without space group, cell parameter or cell volume changes in the studied interval of Ni^{2+}concentration, as mentioned above.

Table 1. Structural properties and Rietveld refinement parameters for cubic $Zn_{2(1-x)}Ni_{2x}TiO_4$, where x =0.00, 0.0007, 0.001, 0.0013, 0.002, and 0.003.

x	0.00	0.0007	0.001	0.0013	0.002	0.003
I) Main phase						
Zn_2TiO_4 (%)	98.46	98.78	98.38	100	100	100
Space group	$Fd\bar{3}m$	$Fd\bar{3}m$	$Fd\bar{3}m$	$Fd\bar{3}m$	$Fd\bar{3}m$	$Fd\bar{3}m$
Crystal system	*Cubic*	*Cubic*	*Cubic*	*Cubic*	*Cubic*	*Cubic*
$a = b = c$ (Å)	8.467(1)	8.471(0)	8.474(5)	8.474(7)	8.474(6)	8.475(2)
V(Å^3)	607.02	607.86	608.61	608.65	608.63	608.76
$(2\theta)_{311}$(deg.)	35.17	35.16	35.15	35.18	35.10	35.10
$FWHM_{(311)}$ (deg.)	0.075	0.127	0.087	0.107	0.132	0.148
$D_{(311)}$(nm)	2139.08	757.56	1412.12	969.74	727.13	624.15
ε x(10^{-3})	0.53	1.51	0.81	1.18	1.58	1.84
δ x(10^{-3})	0.46	1.32	0.71	1.03	1.38	1.60
II) Residual phase						
ZnO (%)	1.54	1.22	1.62	-	-	-
Space group	$P6_{3mc}$	$P6_{3mc}$	$P6_{3mc}$	-	-	-
Crystal system	*Hexagonal*	*Hexagonal*	*Hexagonal*	-	-	-
$a = b$ (Å)	3.249(3)	3.253(6)	3.249(3)	-	-	-
c (Å)	5.207(3)	5.190(5)	5.207(3)	-	-	-
V(Å^3)	47.61	47.58	47.61	-	-	-
III) Agreement factors						
R_{wp}	10.2	11.6	10.5	16.0	11.6	10.8
R_p	10.9	11.4	10.6	25.2	9.7	8.93
R_{exp}	7.15	7.99	7.95	9.0	8.8	9.02
GOF	1.4	1.4	1.3	1.8	1.3	1.2
χ^2	2.05	2.1	1.76	3.17	1.71	1.4

Table 2. Atomic positions obtained from Rietveld refinements.

Atom	Ox State	Wyck Symb	x	y	z
Zn_2TiO_4					
Zn1	+2	8 a	0.125	0.125	0.125
Ti1	+4	16 d	0.500	0.500	0.500
Zn2	+2	16 d	0.500	0.500	0.500
O1	-2	32 e	0.2616(7)	0.2616(7)	0.2616(7)
Zn_2TiO_4: Ni^{2+} (0.07%)					
Zn1	+2	8 a	0.125	0.125	0.125
Ti1	+4	16 d	0.500	0.500	0.500
Zn2	+2	16 d	0.500	0.500	0.500
O1	-2	32 e	0.2572(3)	0.2572(3)	0.2572(3)
Zn_2TiO_4: Ni^{2+} (0.10%)					
Zn1	+2	8 a	0.125	0.125	0.125
Ti1	+4	16 d	0.500	0.500	0.500
Zn2	+2	16 d	0.500	0.500	0.500
O1	-2	32 e	0.2585(2)	0.2585(2)	0.2585(2)
Zn_2TiO_4: Ni^{2+} (0.13%)					
Zn1	+2	8 a	0.125	0.125	0.125
Ti1	+4	16 d	0.500	0.500	0.500
Zn2	+2	16 d	0.500	0.500	0.500
O1	-2	32 e	0.2580(9)	0.2580(9)	0.2580(9)
Zn_2TiO_4: Ni^{2+} (0.20%)					
Zn1	+2	8 a	0.125	0.125	0.125
Ti1	+4	16 d	0.500	0.500	0.500
Zn2	+2	16 d	0.500	0.500	0.500
O1	-2	32 e	0.2581(9)	0.2581(9)	0.2581(9)
Zn_2TiO_4: Ni^{2+} (0.30%)					
Zn1	+2	8 a	0.125	0.125	0.125
Ti1	+4	16 d	0.500	0.500	0.500
Zn2	+2	16 d	0.500	0.500	0.500
O1	-2	32 e	0.2580(4)	0.2580(4)	0.2580(4)

Table 2 shows the atomic positions obtained from Rietveld refinements. Zn^{2+} ions are in two non-equivalent atomic positions: Zn1 in 8a-Wyckoff position (tetrahedral symmetry) and Zn2 in 16d-Wyckoff position (octahedral symmetry). Ti^{4+} ions have the same atomic coordinates as Zn2 ions, showing that the octahedral position is common to the two ions. Therefore, the molecular system can be represented by $[Zn]^{tet}[Zn,Ti]^{oct}O_4$. Ionic compounds as Zn_2TiO_4 are typically neutral. In this way, the charges of the cations balance out the anions charges. The valence states of the elements of the molecular formula are determinate by a condition of maximum stability.

This rule determinates that an ion is more stable when it has eight valence electrons (octet rule). The electronic configuration of the Zn is $[Ar]3d^{10}4s^2$, in which the electron configuration of Argon gas [Ar] has a total of eight electrons ($3s^2\ 3p^6$) in the valence shell. When the Zn atom loses the two electrons of the $4s^2$ shell, becomes the more stable Zn^{2+}cation. The Ti atom with electronic configuration $[Ar]3d^2\ 4s^2$ loses four electrons and became Ti^{4+} with stable electronic configuration [Ar]. The oxygen anions has six electrons in the valence shell (electronic distribution $1s^2\ 2s^2\ 2p^4$). Therefore, it gains two electrons for the 2p shell, achieving the stable valence O^{2-}. In Zn_2TiO_4 formation the raw oxides were, as mentioned in experimental section, $Zn^{2+}O^{2-}$ and $Ti^{4+}O_2^{2-}$, both contain elements in more stable valence states. Therefore, during the $ZnO + TiO_4 \rightarrow Zn_2TiO_4$ processes, the valence is preserved and the electrostatic attraction between cations and oxygen leads to the ionic bond between them. Therefore, as the chemical equilibrium is the stronger condition for ionic solid formation, this fact confirms the valence of the ions Zn^{2+}, Ti^{4+} and O^{2-} in the host.

The crystal radii of the ions in octahedral coordination are: $r_{Ti^{4+}} = 0.745$ Å, $r_{Zn^{2+}} = 0.88$ Å, and $r_{Ni^{2+}} = 0.83$ Å, while in the tetrahedral coordination the crystal radii are $r_{Zn^{2+}} = 0.74$ Å and $r_{Ni^{2+}} = 0.69$ Å[32]. Because of the same valence and similar crystal radii, it is expected that Ni^{2+} ions occupy Zn^{2+} octahedral or/and tetrahedral sites in Zn_2TiO_4. However, the green color of the Zn_2TiO_4:Ni^{2+} sample indicates the occupation of Ni^{2+} ions in octahedral sites[18,33-35].

The green color can be explained as follows. Since the sample has a green color this means that red color is absorbed in sample surface, because the red and the green are complementary colors. Besides this, the green color also means that the light with wavelength in the blue region of the

spectrum is also absorbed at the sample surface. Therefore, the green color is a consequence of the absorption of the red and blue lights by sample surface. The energy absorbed by the Ni^{2+} ion in a coordination complex corresponds to the spacing between the $3d^8$-configuration energy levels involved in the electronic transition. In consequence, the color of the sample also depends upon this spacing. However, this spacing depends on the valence state of the central cation, the cation site symmetry (octahedral or tetrahedral), and the type of ligands (O^{-2}, F^{-1}, Cl^{-1}, for example). When a Ni^{2+} ion is in a strong octahedral crystalline site, the spacing between 3d energy levels (t_{2g} and e_g) is large[35]. Therefore, in this transition, the ion Ni^{2+} absorbs a high-energy radiation, and the color of the sample will be yellow. If this cation is in an octahedral site, weaker than the first example, the spacing between 3d energy levels is smaller than for the earlier case[35] and the absorbed radiation corresponds to the yellow-red region of the spectrum. In consequence, the sample acquires a green color. When the Ni^{2+} ion is in a tetrahedral site, the electronic configuration corresponds to the $3d^2$ in octahedral coordination[34]. The energy levels distribution of $3d^2$ configuration indicates that for weak crystalline field, the spacing between 3d (t_2 and e) energy levels is small. Therefore, the absorbed energy is in the yellow-red region and the samples acquire colors as blue and turquoise, for example[36]. The above considerations allow affirming that the photoluminescence technique is appropriate to identify both, the type and the valence of the emitting substitutional ion, besides the symmetry of the occupation site.

Room temperature X-ray fluorescence (XRF) for (a) Zn_2TiO_4 and (b) Zn_2TiO_4:Ni^{2+} (0.1% of Ni^{2+}) samples (Figure 2) only showed peaks related to the atoms Zn and Ti. The measurements were performed in several regions on the samples' surfaces, with similar results showing the homogeneity of the samples. The lack of Ni^{2+} signal can be explained by the low concentration in the samples.

Figure 3 shows the photoacoustic absorption spectra at room temperature of the $Zn_{2(1-x)}Ni_{2x}TiO_4$, where x = 0.00, 0.0007, 0.001, 0.0013, 0.002 and 0.003. All spectra present a strong absorption below 400 nm that explains the yellow color of the Zn_2TiO_4 sample, because when the color absorbed is the violet, the color seen is yellow. Besides this, all the Zn_2TiO_4:Ni^{2+} samples show an absorption band from 380 nm to 450 nm, and a weak red absorption band. The absorption at red and blue regions of the spectrum explains the green color of samples containing Ni^{2+}.

The photoacoustic spectrum shows all absorber centers in the material, therefore, the band from 380 nm to 450 nm can be attributed to the Ni^{2+} absorbing center in the samples. Because of the strong preference for this kind of site, Ni^{2+} ions occupation in octahedral Zn^{2+} sites are to be expected. But the crystal field transitions[34,35,37] from Ni^{2+} in the photoacoustic spectrum were not observed, because they were strongly overlapped by the absorption of the host. A photoacoustic spectrum similar to that shown in Figure 3 was observed for Zn_2TiO_4 thin films obtained by the sol-gel method[38].

The semiconducting character of the samples was identified using the photoacoustic technique, by determining the energy gap using the Tauc method[39]. The method was originally used for analyses of amorphous materials, but recently its applicability to polycrystalline semiconductor materials was verified[40]. The energy gap can be determined from spectra fitting the photoacoustic data through Equation 1[39]:

$$(\mathrm{PAS}\times h\nu)^n = \alpha(h\nu - \mathrm{E_G}) \quad (1)$$

where PAS is the normalized photoacoustic signal intensity as function of the energy $h\nu$ of the absorbed photon, h is Planck's constant, E_G is the optical gap of the material, α is a proportionality constant and the exponent n characterizes the transition, as such: n = 2 (allowed and direct transitions), 1/2 (allowed and indirect transitions), 2/3 (forbidden and direct transitions) and 1/3 (forbidden and indirect transitions)[41].

Figure 4 shows the plot of the $(\mathrm{PAS}\times h\nu)^N$ against the energy in eV units of the absorbed photon, in which the better result n = 2 is fitted.

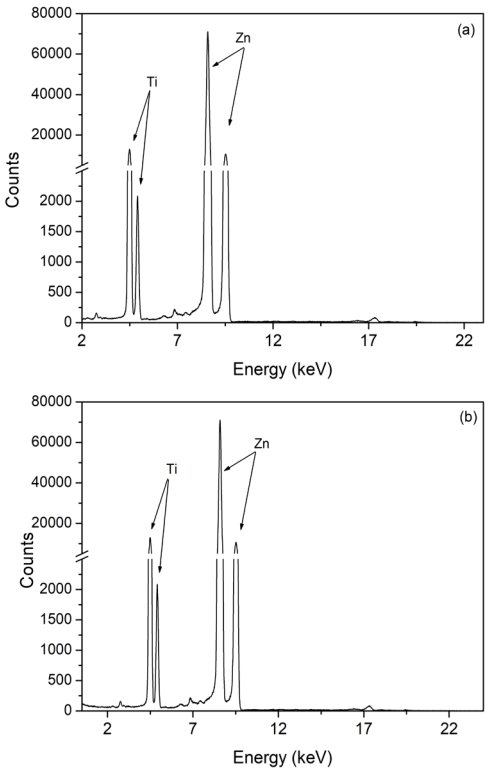

Figure 2. Room temperature X-ray fluorescence (XRF) for (a) Zn_2TiO_4 and (b) Zn_2TiO_4:Ni^{2+} (0.1% of Ni^{2+}).

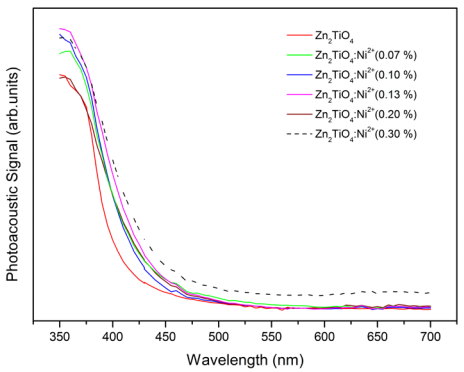

Figure 3. Room temperature photoacoustic absorption spectra of $Zn_{2(1-x)}Ni_{2x}TiO_4$, where x = 0.00, 0.0007, 0.001, 0.0013, 0.002 and 0.003, obtained with an Xe lamp modulated at 10 Hz.

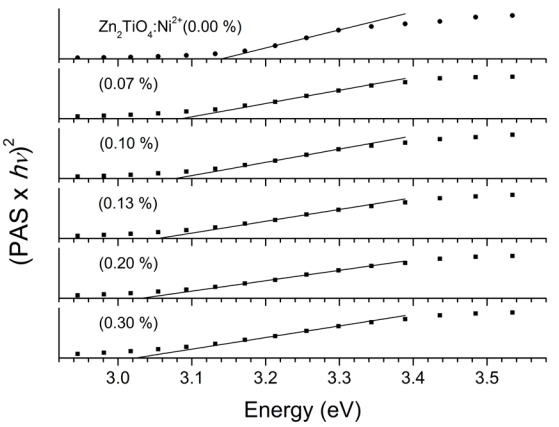

Figure 4. (PAS×$h\nu$)^2 data (black dots) against the energy of the absorbed photon, for $Zn_{2(1-x)}Ni_{2x}TiO_4$, where x = 0.00, 0.0007, 0.001, 0.0013, 0.002 and 0.003. The energy of the absorption transitions were plotted on the horizontal axis. The lines positions on the horizontal axis indicate the bandgap energy of the samples.

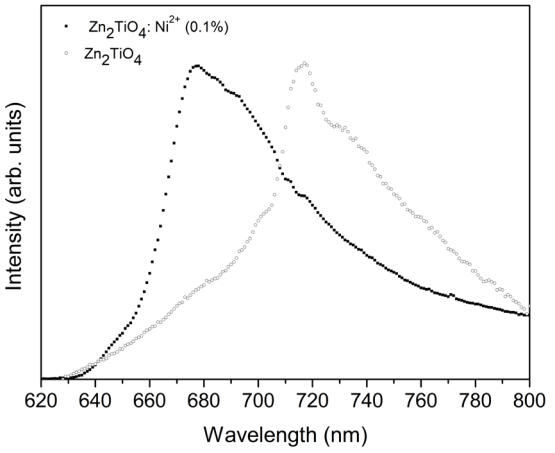

Figure 5. Room temperature emission spectra for Zn_2TiO_4 sample (open circles) and for the Zn_2TiO_4:Ni^{2+} (0.1% of Ni^{2+}) (full squares) excited with 532 nm continuous laser, modulated at 200 Hz.

Therefore, the samples obtained in this work are semiconductors of allowed and direct transition. The bandgap energies obtained for $Zn_{2(1-x)}Ni_{2x}TiO_4$, where x = 0.00, 0.0007, 0.001, 0.0013, 0.002 and 0.003 were 3.140 eV, 3.085 eV, 3.077 eV, 3.054 eV, 3.032 eV, and 3.023 eV, respectively. These values correspond to wavelengths: 394 nm, 402 nm, 403 nm, 406 nm, 409 nm, and 410 nm.

The lowering of the energy gap of the doped sample was also observed for the Zn_2TiO_4:Fe^{3+} [42]. In that paper, Jang et al. showed that Fe^{3+} substitution reduced the bandgap of Zn_2TiO_4 and leads to a photocatalytic activity in the system under visible light irradiation. The lowering of the band gap investigated in this paper would be associated to changes in photoluminescence, as discussed below.

The decreasing of the gap energy with the increasing of substitutional Ni^{2+} concentration could be due to: a) transfer-charge effects from Ni^{2+} to host; b) enhancement of the interactions between orbitals of the localized Ni^{2+} d-electrons and sp-orbitals of Zn^{2+} ions[43]; c) changes in sample surface morphology in consequence of the Ni^{2+} substitutional concentration increasing, that can lead to an enhancement of scattering from surface of the higher energy radiation, followed by a decreasing of the absorption[44], and/or d) creation of a new energy level below the Zn_2TiO_4 conduction band, due to the Ni^{2+} ions. These energy levels lead to absorption of lesser energy photons, which decay through d-d transitions and transitions to the valence band of the host Zn_2TiO_4 [45].

Sometimes when an impurity ion is inserted in a semiconductor, an energy inter-band between the valence and conduction band can arise. In this case, the impurity inserted in the host reduces the energy gap and the optoelectronic properties of the sample are enhanced, as such, there is an improvement to photoluminescence with impurity concentration[46]. In order to verify the way in which the lowering of the band gap in addition with crystallite size (D), micro-strain (ε), and dislocation density (δ) parameters change the emission, photoluminescence spectra are presented in what follows.

Figure 5 shows room temperature phase-resolved emission spectra for the Zn_2TiO_4 sample (open circles) and the Zn_2TiO_4:Ni^{2+} (0.1% Ni^{2+}) (full circles). The spectra were obtained with a continuous 532 nm wavelength laser line chopped at 200 Hz as the excitation source. The 200 Hz chopper frequency is equivalent to a temporal window of 5 ms on and 5 ms off samples illumination. The phase of the signal was adjusted in the lock-in to obtain the maximum signal of the luminescence band observed.

The spectrum of the Zn_2TiO_4 consists of an inhomogeneous broadband extending from 630 nm to 800 nm, with a maximum intensity at 718 nm and weak shoulders at 705 and 730 nm. The inhomogeneous broadening of the emission band can be explained by the degree of disorder of the sample[9].

The spectrum of the Zn_2TiO_4:Ni^{2+} also consists of an inhomogeneous broadband extending from 640 nm to 800 nm with a maximum intensity at 680 nm and weaker shoulders at 690 nm and 718 nm. These shoulders were also observed in the Zn_2TiO_4 sample, therefore, they can be attributed to the host Zn_2TiO_4, while the peak at 680 nm can be assigned to the nickel emission. The band extends beyond 800 nm, outside our experimental limits.

The most common valences of nickel ion are 2+ and 3+. Ni^{3+} ions have a $3d^7$ electronic configuration and their emission is often assigned to bands in the near-infrared region. For example, the ZnO:Ni^{3+} presented a band with maximum intensity at 1.5 μm[47] and the ZnS:Ni^{3+} showed infrared emission from 1.8 μm to 2.2 μm[48], both very far from the emission with barycenter at 680 nm as observed in Figure 5. On the other hand, Ni^{2+} emissions are often observed at the red-infrared region, below 700 nm, therefore, the band with barycenter at 680 nm in the near infrared region is assigned to the $^1T_2(^1D) \rightarrow {}^3T_2(^3F)$ transition of Ni^{2+} ions in octahedral sites[18,34,35,37]. Additional nickel transitions are expected at the green and infrared regions, attributed to the $^1T_2(^1D) \rightarrow {}^3A_2(^3F)$ and $^3T_2(^3F) \rightarrow {}^3A_2(^3F)$ transitions of Ni^{2+} in octahedral sites, respectively. These bands were not observed probably because they are totally overlapped by the host emission, since a broad emission band of Zn_2TiO_4 from 450 nm to 800 nm was observed in reference[8].

As the concentration of ZnO is about 1.6%, which is much higher than Ni^{2+} concentration in the 0.1% Ni^{2+} sample, the possibility of an emission band due to ZnO or ZnO:Ni^{2+} was considered. The emission of ZnO was referred to the blue[49] and green region[50], while emission from ZnO:Ni^{2+} was also reported at blue and green spectral regions[51]. Therefore, the highly probable explanation of the optical properties of the sample is the assignment of these to Ni^{2+} centers in the Zn_2TiO_4 host, because the emission is in the red spectral region.

Figure 6 shows the room temperature time-resolved emission spectra of (a) Zn_2TiO_4 and (b) Zn_2TiO_4:Ni^{2+} (0.1% Ni^{2+}) with excitation radiation from a pulsed Xenon lamp with a repetition rate at 200 Hz, using 360 nm, 480 nm, and 532 nm as excitation wavelengths. Time-resolved emission was obtained in scans with a lamp flash rate of 200 Hz (temporal window of 5 ms), 600 pulses averaged per wavelength and scan step size of 1 nm. All measurements shown in Figure 6a and b were performed under the same instrumental conditions.

Figure 6a shows the most significant spectra among the measurements performed with a wavelength excitation set. The most intense photoluminescence signal was obtained with excitation radiation at a wavelength of 360 nm, where the emission band extends notably further than the measurement limits. The 532 nm wavelength excitation produces an emission band three times less intense than that produced with 360 nm wavelength excitation. These photoluminescence spectra can be attributed to electronic recombination effects, emission from energy levels of structural defects close to the bandgap, and from atomic order-disorder effects[8].

Figure 6b shows the emission of the Zn_2TiO_4:Ni^{2+} (0.1%) sample excited with 360 nm, 480 nm, and 532 nm. The intensity of the band excited with 360 nm decreases to approximately a half-height of the similar band in the Zn_2TiO_4 sample exhibited in Figure 6a. Moreover, the emission band in the sample Zn_2TiO_4 is broader than the emission of the Zn_2TiO_4:Ni^{2+} (0.1%) sample. This fact indicates that: a) some quantity of absorbed energy by Zn_2TiO_4 is transferred from host to Ni^{2+} ions, decreasing the intensity of the emission band; and/or b) Ni^{2+} ions easily absorb the excitation light, and decays to predominantly lower energy levels by non-radiative transitions, leading to a decrease of emission intensity. In Figure 6b a band at 680 nm can also be seen. This band became more intense with 480 nm excitation. Excitation radiation with 360 nm and 532 nm wavelengths favors the emission at 718 nm (from the host) and 680 nm (from the Ni^{2+} centers), respectively. The excitation with 480 nm, in the same way, favors the emission at 680 nm and 718 nm, and 532 nm is the excitation wavelength that favors less the host emission at 718 nm.

In order to verify the emission intensity dependence with Ni^{2+} concentration, room temperature photoluminescence measurements were performed for samples $Zn_{2(1-x)}Ni_{2x}TiO_4$, where x = 0.00, 0.0007, 0.001, 0.0013, 0.002 and 0.003. These values mean that x = 0.0007 (0.07%) of the number of Zn^{2+} ions were substituted for Ni^{2+} ions, and so on up to the x = 0.003 (0.30%) value.

The results are shown in Figure 7. For the measurements, the excitation radiation used was 480 nm, because this wavelength favors both bands at 680 nm (Ni^{2+}) and 718 nm (host), as can be seen in Figure 6b.

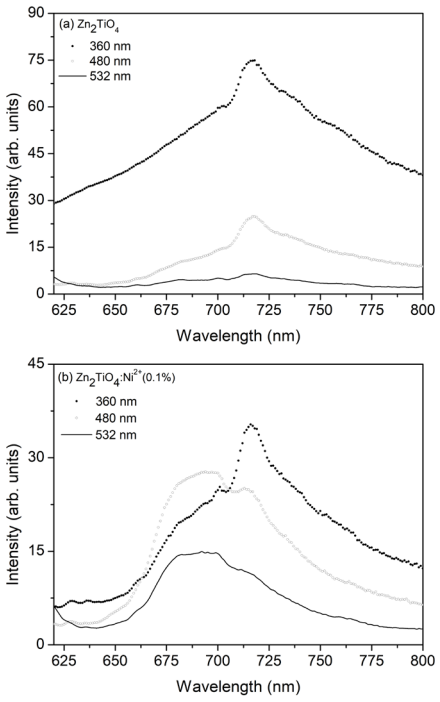

Figure 6. Room temperature time-resolved emission spectra of (a) Zn_2TiO_4 and (b) Zn_2TiO_4:Ni^{2+} (0.1% of Ni^{2+}), both with a lamp repetition rate of 200 Hz, obtained with excitation wavelengths of 360 nm, 480 nm, and 532 nm.

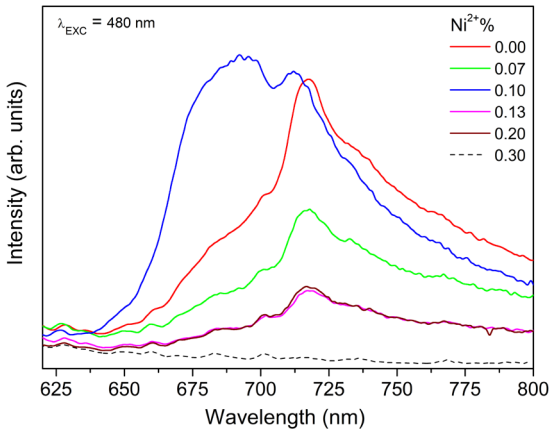

Figure 7. Room temperature emission spectra for $Zn_{2(1-x)}Ni_{2x}TiO_4$, where x = 0.00, 0.0007, 0.001, 0.0013, 0.002 and 0.003. These values mean that 0.07% of Zn^{2+} ions were substituted for Ni^{2+}, and so on up to the 0.30%.

The results will be compared to those shown in Table 1. The X-ray diffraction data showed a decreasing of the quality of crystallization with the increasing of the Ni^{2+} concentration. At the same time, the luminescence intensity was drastically reduced with the Ni^{2+} quantity increasing. It is well-known that the photoluminescence intensity increases/decreases with the increasing/decreasing of the crystallite size[29,52] Therefore, in this work, the reduction of the photoluminescence intensity with the increasing of the Ni^{2+} concentration is in accordance with structural characteristics of samples, since the Ni^{2+} concentration increasing leads to a

lowering of the crystallization quality of the samples. Due to the low Ni^{2+} concentration, the photoluminescence intensity is associated to transitions between d-d states of Ni^{2+} and transitions between Zn_2TiO_4 host and d states of Ni^{2+} ions.

The lowering of the energy of the absorption edge (red shift) of the Ni^{2+} samples, verified in Figure 4, suggests a transfer energy between Zn_2TiO_4 host and d states of Ni^{2+} ions[53]. Furthermore, a decrease in crystallite size indicates a degree of coupling of d orbitals of Ni^{2+} with energy levels of the host[54]. Therefore, the increasing of the Ni^{2+}concentration leads to the lowering of the crystalline quality, which in turn leads to both: a shift of the absorption edge to the red region and a reduction of the photoluminescence intensity.

Figure 7 shows that the higher intensity of photoluminescence emission among the investigated concentrations comes from the 0.1% Ni^{2+} sample excited with 480 nm. The emission of the 0.07% Ni^{2+} sample is lower than the emission of the Zn_2TiO_4 sample. This fact can be explained by taking into consideration that the Ni^{2+} ions are also absorbing centers for the radiation emitted by host Zn_2TiO_4. At the same time, the optimum Ni^{2+} concentration value for photoluminescence was not reached during the interval 0.00%-0.07% of the Ni^{2+} ions. Therefore, the emission intensity of the host was reduced by increasing of Ni^{2+} concentration and the emission from Ni^{2+} transitions is still weak.

However, the emission intensity increase when the Ni^{2+} concentration increases from 0.07% to 0.1% indicates that the radiative relaxation processes of Ni^{2+} become competitive in this concentration interval.

For concentrations higher than 0.1%, the intensity of the whole band decreases, indicating that the weakening of the emission could be due to energy transfer processes between host and Ni^{2+} ions. Due to the low Ni^{2+} concentration, and due to the weak absorption in the spectral region above 500 nm, as can be seen in photoacoustic spectra (Figure 3), the occurrence of Ni^{2+}-Ni^{2+} energy transfer is not expected. In other words, emitting radiation by a Ni^{2+} ion being absorbed by Ni^{2+} neighborhoods' ions is not expected.

Figure 7 also shows that the band at 680 nm (Ni^{2+}) decreases quickly when compared to the band at 718 nm (host), and the whole band decreases with the Ni^{2+} concentration increase. This effect is in accord with the earlier hypothesis about Figure 6b, in which some quantity of absorbed energy by Zn_2TiO_4 is transferred from host to Ni^{2+}, followed by the Ni^{2+} ions decay by predominantly non-radiative transitions, leading to a decrease of emission band intensity. In Figure 7 the Ni^{2+} concentration of 0.30% of Ni^{2+} can be considered as the concentration quenching value for Zn_2TiO_4:Ni^{2+} among the Ni^{2+} concentration investigated in this work.

In the investigation of luminescent material, an important characteristic is the quantum efficiency of the emission. The quantum efficiency (φ) of photoluminescence is defined in Equation 2[55]:

$$\varphi = \frac{n_r}{n_{abs}} \quad (2)$$

where n_r and n_{abs} are the number of emitted and absorbed photons, respectively. The quantum efficiency of Zn_2TiO_4:Ni^{2+} (0.1%) (higher intensity emitting among the Ni^{2+} samples) can be roughly estimated, considering the intensity of the luminescence at 680 nm in Figure 7 and the intensity of the incident light (excitation radiation) which reaches the sample surface as absorbing radiation. The quantum efficiency of emission excited with 480 nm was φ = 0.6, while for the emission excited with 532 nm wavelength the value was φ = 0.3.

Materials in which the energy transitions occur between energy levels with different spin multiplicity (spin-forbidden transitions) in general have quantum efficiency lower than those materials in which the transitions are between energy levels with the same spin multiplicity (spin-allowed)[8]. Also, it is known that low quantum efficiency indicates strong luminescence quenching due to the non-radiative decay processes[56]. However, some spin-forbidden transitions can have high quantum efficiency if non-radiative processes or the interaction between Ni^{2+} ion and host are not significant[46].

The difference between the quantum efficiency of emissions obtained with 480 nm and 532 nm wavelength excitation can be justified: the 480 nm wavelength excited the Ni^{2+} ions and host in the same way, while the 532 nm wavelength excited preferably Ni^{2+} ions. The $^1T_2(^1D) \rightarrow {}^3T_2(^3F)$ transition assigned to the Ni^{2+} emission in this paper is a spin-forbidden transition. Moreover, the emission spectra analysis indicates the possibility of energy transfer processes between Ni^{2+} and Zn_2TiO_4 hosts. Therefore, a lower quantum efficiency of Zn_2TiO_4:Ni^{2+} emission with an excitation wavelength exciting preferably Ni^{2+} ions rather than the Zn_2TiO_4 host is expected. This fact leads to evident losses by non-radiative energy transfers between Ni^{2+} ions and the host.

The quantum efficiency obtained for the Zn_2TiO_4:Dy^{3+} and Zn_2TiO_4:Cr^{3+} were φ = 0.58[46] and 0.53[8], respectively. These values are close to the Zn_2TiO_4:Ni^{2+} value (0.6). This fact indicates that the emission quantum efficiency is due mainly to the host Zn_2TiO_4 radiative processes.

Comparing the quantum efficiency of Zn_2TiO_4:Ni^{2+} (0.1% Ni^{2+}) with those of similar samples, and by the broad and intense emission band, this sample can be considered a possible potential candidate as a tunable active medium at room temperature.

Figures 5-7 show that the Zn_2TiO_4:Ni^{2+} photoluminescence is an overlap of the emissions from the Zn_2TiO_4 host and the emission assigned to the $^1T_2(^1D) \rightarrow {}^3T_2(^3F)$ spin-forbidden transition of Ni^{2+} ions in octahedral sites[18,34,35,37]. Figure 8 shows photoluminescence excitation data for (a) Zn_2TiO_4 and (b) Zn_2TiO_4:Ni^{2+} (0.1% of Ni^{2+})-samples. Time-resolved excitation scans were obtained with a lamp rate of 200 Hz

Table 3. Adjusted parameters and decay time values of Zn_2TiO_4 and Zn_2TiO_4:Ni^{2+}(0.1%).

	A_1	τ_1 (μs)	A_2	τ_2 (μs)	τ (μs)
Zn_2TiO_4	84.53	10.26	-	-	10.26
Zn_2TiO_4:Ni^{2+}(0.1%)	3.91	147.65	12.47	14.31	116.15

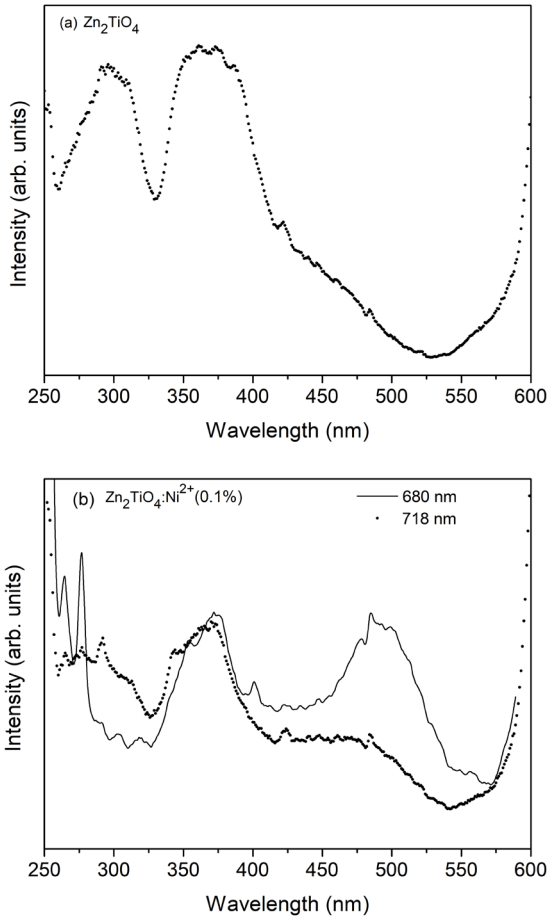

Figure 8. Excitation spectra at room temperature of (a) Zn_2TiO_4 sample monitored at 718 nm and (b) Zn_2TiO_4:Ni^{2+} (0.1% of Ni^{2+}) sample monitored at 680 nm (solid line) and 718 nm (black circles).

(time window of 5 ms), 1 ms signal integration time, 600 pulses averaged per wavelength and a scan step size of 1 nm.

In Figure 8a the absorption edge of Zn_2TiO_4 around 400 nm, is a charge transfer band assigned to the transition of an electron between O^{2-} 2p-orbitals and empty Zn^{2+} 4s-orbitals[42]. The second excitation band at 290 nm was ascribed to the interaction between conduction band electrons and valence band in a charge transfer process between Ti^{4+} 4d-orbitals and O^{2-} 2p-orbitals[57,58]. The excitation spectrum of the Zn_2TiO_4:Ni^{2+} (0.1%) sample (Figure 8b) monitored at 718 nm (black circles) shows similar features to the Zn_2TiO_4 sample monitored at the same wavelength, except for a shoulder in the longer wavelength region. When the emission was monitored at 680 nm, the excitation spectrum showed an additional and intense band of 450 nm to 550 nm, with maximum intensity at 480 nm. This band was assigned to the $^3A_2(^3F) \rightarrow {}^1T_2(^1D)$ spin-forbidden transition of Ni^{2+} ion in the octahedral site[18].

Despite the different electronic configurations of Ni^{2+} and Ni^{3+} (d^8 and d^7, respectively), both can present an overlapping of bands assigned to the Ni^{3+} octahedral, Ni^{3+} tetrahedral, and Ni^{2+} octahedral coordination[34,35,37] in the spectral region from 400 nm to 500 nm.

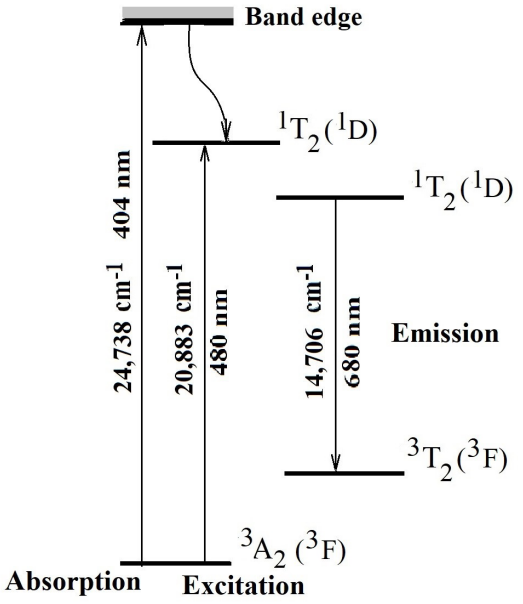

Figure 9. Energy levels diagram of the Zn_2TiO_4:Ni^{2+} (0.1% of Ni^{2+}) transitions.

In this paper, based on the shape and energy of the observed $^1T_2(^1D) \rightarrow {}^3T_2(^3F)$ emission band, the excitation band at 480 nm was assigned to $^3A_2(^3F) \rightarrow {}^1T_2(^1D)$ transition of Ni^{2+} ions in octahedral sites.

The energy diagram of Zn_2TiO_4:Ni^{2+}(0.1%) transitions is shown in Figure 9, in which: the absorption energy for band edge (photoacoustic spectra, Figure 4, at 3.08 eV) is 24,738 cm^{-1} (404 nm); the excitation in Figure 8 (excitation spectra), shows energy at 20,883 cm^{-1} (480 nm); and finally the red emission at 680 nm (14,706 cm^{-1}).

The comparison of photoluminescence and excitation spectra of Zn_2TiO_4 and Zn_2TiO_4:Ni^{2+} (0.1%) samples leads to the conclusion that in the samples which contain Ni^{2+} as a substitutional impurity, the energy processes are assigned to two reasons: the transitions in the host Zn_2TiO_4 and the d-d transitions of Ni^{2+} ions. The assignment of an emission with a two decay pathway can be confirmed through photoluminescence decay measurements because different energy relaxation processes have characteristic decay times.

The results for the decay time experiments are shown in Figure 10, in which one can see the time dependence of photoluminescence intensity at room temperature for 718 nm wavelength, excited with 360 nm of (a) Zn_2TiO_4 and (b) Zn_2TiO_4:Ni^{2+} (0.1%).

Photoluminescence intensity decay of the Zn_2TiO_4 sample (Figure 10a) was fitted by a simple exponential function, while the decay of the Zn_2TiO_4:Ni^{2+}(0.1%) sample (Figure 10b) was fitted by a bi-exponential function, described by Equation 3:

$$I(t) = A_1 e^{-t/\tau_1} + A_2 e^{-t/\tau_2} \quad (3)$$

The excitation and emission wavelengths were chosen in order to determine how the Ni^{2+} insertion changes the host decay time.

The bi-exponential decay shows that the Zn_2TiO_4:Ni^{2+} (0.1%) sample has two decay paths[59]. It is important to

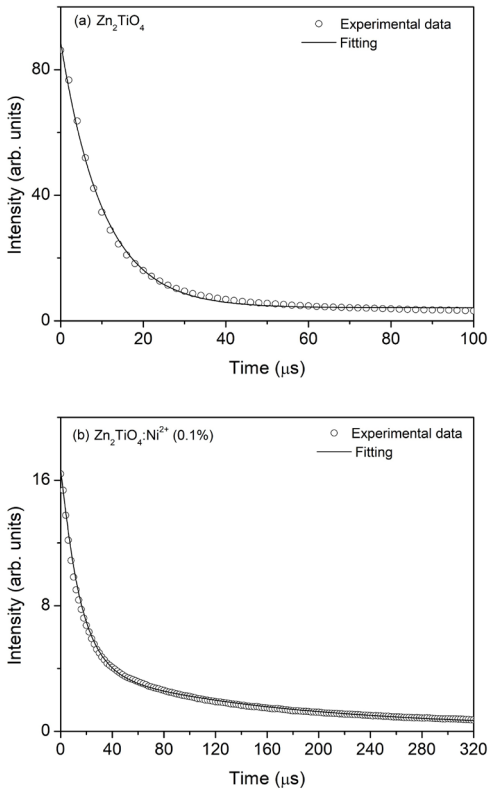

Figure 10. Photoluminescence decay time at room temperature excited with 360 nm and monitored at 718 nm of (a) Zn_2TiO_4 and (b) $Zn_2TiO_4:Ni^{2+}$ (0.1% of Ni^{2+}).

note that the decay times τ_1 and τ_2 are both functions of the coupling between the emitting centers, as well as functions of the number of the emitted photons in each decay path, defined by the weights A_1 and A_2. The decay time average τ of a bi-exponential function can be obtained from Equation 4[60].

$$\tau = \frac{A_1\tau_1^2 + A_2\tau_2^2}{A_1\tau_1 + A_2\tau_2} \quad (4)$$

The parameters A_1 and A_2 and decay times τ_1, τ_2 and τ, are listed in Table 3. The emission decay time of the Zn_2TiO_4 is about 10μs. This short decay time is due to the influence of the shorter electron-hole recombination in the decay process.

However, the decay of the $Zn_2TiO_4:Ni^{2+}$ (0.1% Ni^{2+}) sample is a bi-exponential decay in which the shorter value τ_2 can be assigned mainly to the relaxation from the conduction band to the valence band of Zn_2TiO_4, because this value is close to the time decay obtained for the Zn_2TiO_4 sample. Furthermore, the longer decay time τ_1 can be attributed mainly to the spin-forbidden transitions between d-d energy levels of Ni^{2+} in octahedral sites[18,34,35,37]. Therefore, decay times τ_1 and τ_2 are both functions of the coupling between Zn_2TiO_4 host and Ni^{2+} emissions. The average lifetime τ of the $Zn_2TiO_4:Ni^{2+}$ (0.1%) sample is close to the longer decay time component because there are large differences between the two decay time components. The decay time of the most intense emission (at 718 nm) of both Zn_2TiO_4 and $Zn_2TiO_4:Ni^{2+}$ (0.1%)-samples, is in accord with the statement of the emission band of the doped sample, having an overlap of transitions of Zn_2TiO_4 with d-d transitions of Ni^{2+} ions in octahedral sites.

4. Conclusions

This work investigated the structural, optical and energy level features of $Zn_{2(1-x)}Ni_{2x}TiO_4$, where x = 0.00, 0.0007, 0.001, 0.0013, 0.002 and 0.003, in which Zn^{2+} ions were replaced by Ni^{2+} ions. The Ni samples present a broad emission band from 600 nm to 800 nm, and the intensity of emission at 800 nm indicates that this band extends to a higher wavelength. The emission band is an overlap of host transitions and d-d transitions of Ni^{2+} in octahedral sites. Because of the strong overlap, the two different contributions were not fully separated by light excitation or phase-signal selection. The photoluminescence intensity of the Zn_2TiO_4 is higher than $Zn_2TiO_4:Ni^{2+}$. Therefore, the excited energy levels of Ni^{2+} are probably partially populated by electrons from the Zn_2TiO_4 conduction band, which decay to excited energy levels of the Ni^{2+} ions. The intensity of photoluminescence decreases with Ni^{2+} concentration and the concentration quenching is reached even at a low Ni^{2+} concentration. The decrease of emission intensity when Ni^{2+} is inserted in Zn_2TiO_4, shows that, in this case, the lowering of the bandgap does not contribute to the efficiency of the emission.

Analyzing the quantum efficiency and the broad, high intensity of the emission band of $Zn_2TiO_4:Ni^{2+}$ (0.1%), it is possible to consider this sample as a potential candidate as radiation tunable active medium at room temperature.

5. Acknowledgments

This study was financed in part by the Coordenação de Aperfeiçamento de Pessoal de Nível Superior – Brasil (CAPES) - Finance Code 001. The authors are also grateful to Fundação Carlos Chagas Filho de Amparo à Pesquisa do Estado do Rio de Janeiro (FAPERJ) and Conselho Nacional de Desenvolvimento Científico e Tecnológico (CNPq) for their financial support; and to the LIETA/IFADT/UERJ for XRD and XRF data. S. S. Pedro and L. P. Sosman thank CNPq for the Research Productivity fellowships. S. S. Pedro gives thanks to the Jovem Cientista do Nosso Estado (JCNE-FAPERJ) fellowship.

6. References

1. Marin SJ, O'Keeffe M, Partin DE. Structures and crystal chemistry of ordered spinels: $LiFe_5O_8$, $LiZnNbO_4$, and Zn_2TiO_4. J Solid State Chem. 1994;113(2):413-9. http://dx.doi.org/10.1006/jssc.1994.1389.
2. Fenoll J, Garrido I, Hellín P, Flores P, Vela N, Navarro S. Photocatalytic oxidation of pirimicarb in aqueous slurries containing binary and ternary oxides of zinc and titanium. J Photochem Photobiol Chem. 2015;298:24-32. http://dx.doi.org/10.1016/j.jphotochem.2014.10.014.
3. Antoniou MG, Shoemaker JA, Cruz AA, Dionysiou DD. Unveiling new degradation intermediates/pathways from the photocatalytic degradation of microcystin-LR. Environ Sci Technol. 2008;42(23):8877-83. http://dx.doi.org/10.1021/es801637z. PMid:19192812.
4. Obradovic N, Labus N, Sreckovic T, Stevanovic S. Reaction sintering of the 2ZnO -TiO_2 system. Sci Sinter. 2007;39(2):127-32. http://dx.doi.org/10.2298/SOS0702127O.

5. Ghanbarnezhad S, Nemati A, Naghizadeh R. Low temperature synthesis of zinc-titanate ultra fine powders. APCBEE Procedia. 2013;5:6-10. http://dx.doi.org/10.1016/j.apcbee.2013.05.002.
6. Ohsato H. Microwave materials with high Q and low dielectric constant for wireless communications. MRS Proceedings. 2004;833:G2.4. http://dx.doi.org/10.1557/PROC-833-G2.4.
7. Kim HT, Kim Y, Valant M, Suvorov D. Titanium incorporation in Zn_2TiO_4 spinel ceramics. J Am Ceram Soc. 2001;84(5):1081-6. http://dx.doi.org/10.1111/j.1151-2916.2001.tb00793.x.
8. Chaves AC, Lima SJG, Araújo RCMU, Maurera MAMA, Longo E, Pizani PS, et al. Photoluminescence in disordered Zn_2TiO_4. J Solid State Chem. 2006;179(4):985-92. http://dx.doi.org/10.1016/j.jssc.2005.12.018.
9. Sosman LP, López A, Camara AR, Pedro SS, Carvalho ICS, Cella N. Optical and structural properties of Zn_2TiO_4:Mn^{2+}. J Electron Mater. 2017;46(12):6848-55. http://dx.doi.org/10.1007/s11664-017-5742-z.
10. Espinoza VAA, López A, Neumann R, Sosman LP, Pedro SS. Photoluminescence of divalent cobalt ions in tetrahedral sites of zinc orthotitanate. J Alloys Compd. 2017;720:417-22. http://dx.doi.org/10.1016/j.jallcom.2017.05.188.
11. Girish KM, Prashantha SC, Naik R, Nagabhushana H. Zn_2TiO_4: a novel host lattice for Sm^{3+} doped reddish orange light emitting photoluminescent material for thermal and fingerprint sensor. Opt Mater. 2017;73:197-205. http://dx.doi.org/10.1016/j.optmat.2017.08.009.
12. Iverson MV, Windscheif JC, Sibley WA. Optical parameters for the MgO:Ni^{2+} laser system. Appl Phys Lett. 1980;36(3):183-4. http://dx.doi.org/10.1063/1.91439.
13. Kück S. Laser-related spectroscopy of ion-doped crystals for tunable solid-state laser. Appl Phys B. 2001;72(5):515-62. http://dx.doi.org/10.1007/s003400100540.
14. Zhang Y, Li X, Lai Z, Zhang R, Lewis E, Azmi AI, et al. Largest enhancement of broadband near-infrared emission of Ni^{2+} in transparent nanoglass ceramics: using Nd^{3+} as a sensitizer and Yb^{3+} as an energy-transfer bridge. J Phys Chem C. 2019;123(15):10021-7. http://dx.doi.org/10.1021/acs.jpcc.9b00359.
15. Gao Z, Liu Y, Ren J, Fang Z, Lu X, Lewis E, et al. Selective doping of Ni^{2+} in highly transparent glass-ceramics containing nano-spinels $ZnGa_2O_4$ and $Zn_{1+x}Ga_{2-2x}Ge_xO_4$ for broadband near-infrared fiber amplifiers. Sci Rep. 2017;7(1):1783. http://dx.doi.org/10.1038/s41598-017-01676-6. PMid:28496207.
16. Hari Krishna R, Nagabhushana BM, Nagabhushana H, Monika DL, Sivaramakrishna R, Shivakumara C, et al. Photoluminescence, thermoluminescence and EPR studies of solvothermally derived Ni^{2+} doped $Y(OH)_3$ and Y_2O_3 multi-particle-chain microrods. J Lumin. 2014;155:125-34. http://dx.doi.org/10.1016/j.jlumin.2014.06.019.
17. Koteswara Rao K, Rao MC. Optical and luminescent properties of Ni^{2+} doped PVA capped CdTe nanoparticles. Rasayan J Chem. 2017;10:904-9.
18. Costa GKB, Sosman LP, López A, Cella N, Barthem RB. Optical and structural properties of Ni^{2+}-doped magnesium gallate polycrystalline samples. J Alloys Compd. 2012;534:110-4. http://dx.doi.org/10.1016/j.jallcom.2012.04.039.
19. Sigaev VN, Golubev NV, Ignateva ES, Savinkov VI, Campione M, Lorenzi R, et al. Nickel-assisted growth and selective doping of spinel-like gallium oxide nanocrystals in germano-silicate glasses for infrared broadband light emission. Nanotechnology. 2012;23(1):015708. http://dx.doi.org/10.1088/0957-4484/23/1/015708. PMid:22155977.
20. Xing YJ, Borguet E. Specificity and sensitivity of fluorescence labeling of surface species. Langmuir. 2007;23(2):684-8. http://dx.doi.org/10.1021/la060994s. PMid:17209620.
21. Ivanov VB, Behnisch J, Holländer A, Mehdorn F, Zimmermann H. Determination of functional groups on polymer surfaces using fluorescence labelling. Surf Interface Anal. 1996;24(4):257-62. http://dx.doi.org/10.1002/(SICI)1096-9918(199604)24:4<257::AID-SIA107>3.0.CO;2-1.
22. Fernández A, Alonso JR, Flores JL, Ayubi GA, Di Martino JM, Ferrari JA. Optical processing of color images with incoherent illumination: orientation-selective edge enhancement using a modified liquid crystal display. Opt Express. 2011;19(21):21091-7. http://dx.doi.org/10.1364/OE.19.021091. PMid:21997117.
23. FullProf Suite. Crystallographics tools for Rietveld, profile matching & integrated intensity refinements of X-ray and/or neutron data [Internet]. 2006 [cited 2019 May 7]. Available from: http://www.ill.eu/sites/fullprof/
24. International Centre for Diffraction Data – ICDD. Card International Centre for Diffraction Data. Newtown Square: ICDD; 2002.
25. Millard RL, Peterson RC, Hunter BK. Study of the cubic to tetragonal transition in Mg_2TiO_4 and Zn_2TiO_4 spinels by 17O MAS NMR and Rietveld refinement of X-ray diffraction data. Am Mineral. 1995;80(9-10):885-96. http://dx.doi.org/10.2138/am-1995-9-1003.
26. García-Martínez O, Rojas RM, Vila E, Martín de Vidales JL. Microstructural characterization of nanocrystals of ZnO and CuO obtained from basic salts. Solid State Ion. 1993;63-65:442-9. http://dx.doi.org/10.1016/0167-2738(93)90142-P.
27. Lokesh B, Rao NM. Effect of Cu-doping on structural, optical and photoluminescence properties of zinc titanates synthesized by solid state reaction. J Mater Sci Mater Electron. 2016;27(5):4253-8. http://dx.doi.org/10.1007/s10854-016-4290-2.
28. Goktas A. Role of simultaneous substitution of Cu^{2+} and Mn^{2+} in ZnS thin films: defects-induced enhanced room temperature ferromagnetism and photoluminescence. Physica E. 2020;117:113828. http://dx.doi.org/10.1016/j.physe.2019.113828.
29. Shekharam T, Siddarth J, Reddy YV, Nagabhushanam M. Photoluminescence studies of $Cd_{0.8-x}Pb_xZn_{0.2}S$ semiconductor compounds. J Lumin. 2018;197:56-61. http://dx.doi.org/10.1016/j.jlumin.2017.12.067.
30. Goktas A, Tumbul A, Aba Z, Durgun M. Mg doping levels and annealing temperature induced structural, optical and electrical properties of highly c-axis oriented ZnO:Mg thin films and Al/ZnO:Mg/p-Si/Al heterojunction diode. Thin Solid Films. 2019;680:20-30. http://dx.doi.org/10.1016/j.tsf.2019.04.024.
31. Joishy S, Antony A, Poornesh P, Choudhary RJ, Rajendra BV. Influence of Cd on structure, surface morphology, optical and electrical properties of nano crystalline ZnS films. Sens Actuators A Phys. 2020;303:111719. http://dx.doi.org/10.1016/j.sna.2019.111719.
32. Shannon RD. Revised effective ionic radii and systematic studies of interatomic distances in halides and chalcogenides. Acta Crystallogr. 1976;32(5):751-67. http://dx.doi.org/10.1107/S0567739476001551.
33. Roselina NRN, Azizan A. Ni nanoparticles: study of particles formation and agglomeration. Procedia Eng. 2012;41:1620-6. http://dx.doi.org/10.1016/j.proeng.2012.07.359.
34. Tanabe Y, Sugano S. On the absorption spectra of complex ions, I. J Phys Soc Jpn. 1954;9(5):753-66. http://dx.doi.org/10.1143/JPSJ.9.753.
35. Tanabe Y, Sugano S. On the absorption spectra of complex ions, II. J Phys Soc Jpn. 1954;9(5):766-79. http://dx.doi.org/10.1143/JPSJ.9.766.
36. Bhim A, Laha S, Gopalakrishnan J, Natarajan S. Color tuning in garnet oxides: the role of tetrahedral coordination geometry for 3 D metal ions and ligand-metal charge transfer (band gap manipulation). Chem Asian J. 2017;12(20):2734-43. http://dx.doi.org/10.1002/asia.201701040. PMid:28868809.
37. Tanabe Y, Sugano S. On the absorption spectra of complex ions, III. The calculation of the crystalline field strength. J Phys Soc Jpn. 1956;11(8):864-77. http://dx.doi.org/10.1143/JPSJ.11.864.
38. Mayén-Hernández SA, Torres-Delgado G, Castanedo-Pérez R, Villarreal MG, Cruz-Orea A, Alvarez JGM, et al. Optical and

structural properties of ZnO + Zn_2TiO_4 thin films prepared by the sol–gel method. J Mater Sci Mater Electron. 2007;18(11):1127-30. http://dx.doi.org/10.1007/s10854-007-9267-8.

39. Tauc J, Grigorovici R, Vancu A. Optical properties and electronic structure of amorphous germanium. Phys Status Solidi, B Basic Res. 1966;15(2):627-37. http://dx.doi.org/10.1002/pssb.19660150224.
40. Viezbicke BD, Patel S, Davis BE, Birnie DP 3rd. Evaluation of the Tauc method for optical absorption edge determination: ZnO thin films as a model system. Phys Status Solidi, B Basic Res. 2015;252(8):1700-10. http://dx.doi.org/10.1002/pssb.201552007.
41. García-Ramírez E, Mondragón-Chaparro M, Zelaya-Angel O. Bandgap coupling in photocatalytic activity in ZnO-TiO_2 thin films. Appl Phys, A Mater Sci Process. 2012;108(2):291-7. http://dx.doi.org/10.1007/s00339-012-6890-x.
42. Jang JS, Borse PH, Lee JS, Lim KT, Jung OS, Jeong ED, et al. Energy band structure and photocatalytic property of Fe-doped Zn_2TiO_4 material. Bull Korean Chem Soc. 2009;30(12):3021-4. http://dx.doi.org/10.5012/bkcs.2009.30.12.3021.
43. Goktas A. High-quality solution-based Co and Cu co-doped ZnO nanocrystalline thin films: comparison of the effects of air and argon annealing environments. J Alloys Compd. 2018;735:2038-45. http://dx.doi.org/10.1016/j.jallcom.2017.11.391.
44. Tumbul A, Aslan F, Demirozu S, Goktas A, Kilic A, Durgun M, et al. Solution processed boron doped ZnO thin films: influence of different boron complexes. Mater Res Express. 2018;6(3):035903. http://dx.doi.org/10.1088/2053-1591/aaf4d8.
45. Cahyaningsih D, Taufik A, Saleh R. Effect of Ni doping on the structural and optical properties of TiO_2 nanoparticles prepared by co-precipitation method. J Phys Conf Ser. 2020;1442:012017. http://dx.doi.org/10.1088/1742-6596/1442/1/012017.
46. Girish KM, Prashantha SC, Nagabhushana H. Facile combustion based engineering of novel white light emitting Zn_2TiO_4:Dy^{3+} nanophosphors for display and forensic applications. J Sci Adv Mater Devices. 2017;2:360-70.
47. Thurian P, Heitz R, Hoffmann A, Broser I. Nonlinear Zeeman effect of the Ni^{3+} centre in ZnO. J Cryst Growth. 1992;117(1-4):727-31. http://dx.doi.org/10.1016/0022-0248(92)90845-A.
48. Goetz G, Schulz HJ. Kinetics of the formation of $Ni^{3+}(3d^7)$ ions in ZnS and their detection by near-infrared emission. J Lumin. 1988;40-41:311-2. http://dx.doi.org/10.1016/0022-2313(88)90208-6.
49. Ding J, Chen H, Fu H. Defect-related photoluminescence emission from annealed ZnO films deposited on AlN substrates. Mater Res Bull. 2017;95:185-9. http://dx.doi.org/10.1016/j.materresbull.2017.07.042.
50. Chunduri LAA, Kurdekar A, Pradeep BE, Haleyurgirisetty MK, Venkataramaniah K, Hewlett IK. Streptavidin conjugated ZnO nanoparticles for early detection of HIV infection. Advanced Materials Letters. 2017;8(4):472-80. http://dx.doi.org/10.5185/amlett.2017.6579.
51. Samanta A, Goswami MN, Mahapatra PK. Magnetic and electric properties of Ni-doped ZnO nanoparticles exhibit diluted magnetic semiconductor in nature. J Alloys Compd. 2018;730:399-407. http://dx.doi.org/10.1016/j.jallcom.2017.09.334.
52. Wang WN, Widiyastuti W, Ogi T, Lenggoro IW, Okuyama K. Correlations between crystallite/particle size and photoluminescence properties of submicrometer phosphors. Chem Mater. 2007;19(7):1723-30. http://dx.doi.org/10.1021/cm062887p.
53. Sakthivel P, Muthukumaran S, Ashokkumar M. Structural, band gap and photoluminescence behaviour of Mn-doped ZnS quantum dots annealed under Ar atmosphere. J Mater Sci Mater Electron. 2015;26(3):1533-42. http://dx.doi.org/10.1007/s10854-014-2572-0.
54. Bhargava RN, Gallagher D, Hong X, Nurmikko A. Optical properties of manganese-doped nanocrystals of ZnS. Phys Rev Lett. 1994;72(3):416-9. http://dx.doi.org/10.1103/PhysRevLett.72.416. PMid:10056425.
55. Kück S, Petermann K, Pohlmann U, Huber G. Near-infrared emission of Cr^{4+}-doped garnets: Lifetimes, quantum efficiencies, and emission cross sections. Phys Rev B Condens Matter. 1995;51(24):17323-31. http://dx.doi.org/10.1103/PhysRevB.51.17323. PMid:9978759.
56. Kuleshov NV, Mikhailov VP, Scherbitsky VG, Prokoshin PV, Yumashev KV. Absorption and luminescence of tetrahedral Co^{2+} ion in $MgAl_2O_4$. J Lumin. 1993;55(5-6):265-9. http://dx.doi.org/10.1016/0022-2313(93)90021-E.
57. Andrade LHC, Lima SM, Novatski A, Neto AM, Bento AC, Baesso ML, et al. Spectroscopic assignments of Ti^{3+} and Ti^{4+} in titanium-doped OH-free low-silica calcium aluminosilicate glass and role of structural defects on the observed long lifetime and high fluorescence of Ti^{3+} ions. Phys Rev B Condens Matter Mater Phys. 2008;78(22):224202. http://dx.doi.org/10.1103/PhysRevB.78.224202.
58. Yamaga M, Yosida T, Hara S, Kodama N, Henderson B. Optical and electron spin resonance spectroscopy of Ti^{3+} and Ti^{4+} in Al_2O_3. J Appl Phys. 1994;75(2):1111-7. http://dx.doi.org/10.1063/1.356494.
59. Lyvers DP, Moazzezi M, de Silva VC, Brown DP, Urbas AM, Rostovtsev YV, et al. Cooperative bi-exponential decay of dye emission coupled via plasmons. Sci Rep. 2018;8(1):9508. http://dx.doi.org/10.1038/s41598-018-27901-4. PMid:29934509.
60. Okabe K, Inada N, Gota C, Harada Y, Funatsu T, Uchiyama S. Intracellular temperature mapping with a fluorescent polymeric thermometer and fluorescence lifetime imaging microscopy. Nat Commun. 2012;3(1):705. http://dx.doi.org/10.1038/ncomms1714. PMid:22426226.